

# Entanglement Entropy on Generalized Brillouin Zone

Zhenghao Yang,<sup>1</sup> Chaoze Lu,<sup>1</sup> and Xiancong Lu<sup>1,\*</sup>

<sup>1</sup>*Department of Physics, Xiamen University, Xiamen 361005, China*

We investigate the entanglement properties of non-Hermitian Su-Schrieffer-Heeger (SSH) model from the perspective of the Generalized Brillouin Zone (GBZ). The non-Bloch entanglement entropy is defined on a quasi-reciprocal lattice, obtained by performing an ordinary Fourier transformation on the non-Bloch Hamiltonian. We demonstrate that the broken bulk-boundary correspondence is recovered in terms of the non-Bloch entanglement entropy. When the GBZ is circular, we show that the non-Bloch entanglement entropy is well-defined (real and positive-definite) in large parameter regions, except close to the exceptional points (EPs). In the critical region, we found that each Fermi point contributes precisely 1 to the central charge  $c$  of the logarithmic scaling. At the EP, the central charge becomes negative due to the presence of the exceptional bound state. For the case of non-circular GBZ, long-range hopping emerges in the quasi-reciprocal lattice, and the von Neumann entropy on the GBZ is no longer real. However, the non-Bloch edge entanglement entropy remains real, which serves as a reliable topological indicator and respects the bulk-boundary correspondence. We compute the topological phase diagram, and reveal the critical behavior along the exceptional phase boundaries.

## I. INTRODUCTION

Non-Hermitian quantum mechanics naturally arises from the study of open quantum systems coupling with an external environment [1, 2]. For non-Hermitian systems with nonreciprocal hoppings, the bulk eigenstates under open boundary conditions (OBC) accumulate at boundaries, which is named by the non-Hermitian skin effect (NHSE) [3–6] and has been extensively studied recently [7, 8]. In the presence of NHSE, the energy spectrum sensitively depends on the boundary conditions: the energy spectrum under OBC forms a star-shaped branching figures [9], while the energy spectrum under periodic boundary conditions (PBC) makes up loops enclosing the OBC spectrum [10, 11]. The NHSE also results in the breakdown of the celebrated bulk-boundary correspondence (BBC) of topological band theory [12, 13]: the transition points of bulk topological invariants do not match with transition points of zero modes under OBC [3, 14, 15]. In order to understand the topology of non-Hermitian systems, the non-Bloch band theory and the generalized Brillouin zone (GBZ) are proposed, based on which the BBC for non-Hermitian systems can be reestablished [3, 16, 17]. Motivated by this breakthrough, the non-Bloch band theory has been widely used, e.g., to construct Green function [18], to investigate the dynamical phenomena [19] and the non-Bloch parity-time symmetry [20].

Quantum entanglement offers a unique perspective on the exotic phases and phase transitions of Hermitian quantum many-body systems [21, 22]. The degree of entanglement is quantified by the entanglement entropy (EE), which can be obtained by partitioning the system into several subsystems. Importantly, the topological EE is the quantity to characterize the topological order of a

gapped system [23, 24]. For the one-dimensional (1D) Hermitian critical (gapless) system, the scaling behavior of EE with the size of subsystem contains valuable information about the critical point, such as the central charge of the unitary conformal field theory (CFT) [25, 26].

The entanglement properties of the non-Hermitian quantum systems is also an interesting topic which has attracted many attentions recently [27–47]. The conception of EE has been generalized to the non-Hermitian systems in the biorthogonal basis [28, 29]. A logarithmic scaling with central charge  $c = -2$  is found at critical point of the non-Hermitian Su-Schrieffer-Heeger (SSH) model, which can be explained by the  $bc$ -ghost non-unitary CFT [29, 38]. However, the physical meaning of EE remains somewhat ambiguous in this straightforward generalization [38, 40]: The eigenvalues of reduced density matrix  $\rho_A$  are no longer positive definite, which leads to a negative or even complex EE. This is inconsistent with the probability interpretation of a measurable quantity [38, 40]. Some attempts have been made to remedy this situation, for example, the generic entanglement entropy  $S_A = -\text{Tr}(\rho_A \ln |\rho_A|)$  is proposed in Ref. [38], the modified partial trace formalism is introduced in Ref. [27]. However, more systematic analysis is needed in this direction.

Inspired by the success of non-Hermitian topological band theory in terms of GBZ, we may ask whether it is possible to construct an EE on the GBZ which has proper behaviors? We address this question in this paper for the non-Hermitian systems with skin effect. We begin with a GBZ Hamiltonian and then make a Fourier transformation to obtain a quasi-reciprocal lattice [48]. The entanglement entropy on GBZ is calculated by partitioning this quasi-reciprocal lattice. The behaviors of various EE will be examined for two types of GBZ (circular or non-circular). Our study may shed light on the physical meanings of GBZ and non-Hermitian EE, and also open the possibility to study the many-body physics based on GBZ.

\* xlu@xmu.edu.cn

This paper is organized as the following: In Sec. II, we review the basic notions of biorthogonal entanglement entropy. In Sec. III, we introduce the non-Hermitian SSH model and the quasi-reciprocal lattice, on which the entanglement entropy is calculated. In Sec. IV, we present the results of entanglement entropy on the circular GBZ. In Sec. V, we present the results of entanglement entropy on the non-circular GBZ. Finally, a brief summary and discussion are provided in Sec. VI.

## II. BIORTHOGONAL ENTANGLEMENT ENTROPY

We consider a diagonalizable non-Hermitian Hamiltonian  $\mathcal{H} = \sum_{i,j} c_i^\dagger H_{ij} c_j$  with  $\mathcal{H} \neq \mathcal{H}^\dagger$ . Here,  $c_i^\dagger (c_i)$  is the fermionic creation (annihilation) operator (on lattice site  $i$ ) satisfying the usual anticommutation relation  $\{c_i, c_j^\dagger\} = \delta_{i,j}$ ,  $\{c_i, c_j\} = 0$ , and  $H_{ij}$  denotes the element of a hopping matrix. In the framework of biorthogonal quantum mechanics [49], the Hamiltonian  $\mathcal{H}$  has two types of eigenvectors

$$\mathcal{H}|R_n\rangle = E_n|R_n\rangle, \quad \mathcal{H}^\dagger|L_n\rangle = E_n^*|L_n\rangle, \quad (1)$$

where  $|L_n\rangle$  and  $|R_n\rangle$  are referred to the left and right eigenvectors, respectively, and are required to satisfy the biorthonormality condition  $\langle L_m|R_n\rangle = \delta_{mn}$ . The Hamiltonian  $\mathcal{H}$  can be diagonalized as  $\mathcal{H} = \sum_n E_n d_{Rn}^\dagger d_{Ln}$ , with the creation operator  $d_{Rn}^\dagger$  ( $d_{Ln}^\dagger$ ) being related to the eigenstate  $|R_n\rangle$  ( $|L_n\rangle$ ). Due to the non-Hermiticity,  $d_{Ln}^\dagger \neq (d_{Rn})^\dagger$ , but the following anticommutation relations still hold [28, 29, 36]:  $\{d_{Lm}^\dagger, d_{Rn}\} = \delta_{mn}$ ,  $\{d_{Lm}^\dagger, d_{Ln}^\dagger\} = \{d_{Rm}, d_{Rn}\} = 0$ . The transformation between quasiparticle operators and the original lattice operators is

$$\begin{aligned} d_{Rn}^\dagger &= \sum_i c_i^\dagger V_{in}, \quad V_{in} = \langle i|R_n\rangle \\ d_{Lm} &= \sum_j W_{mj}^\dagger c_j, \quad W_{jm} = \langle j|L_m\rangle \end{aligned} \quad (2)$$

in which the transformation matrices  $V$  and  $W$  meet the condition  $W^\dagger V = 1$  (*i.e.*,  $W^\dagger = V^{-1}$ ).

When the energy of non-Hermitian systems is complex, there are different ways to define the many-body ground state. In this paper, we construct the many-body ground states by filling up the levels to Fermi energy according to the real part of the energy [28–30, 36, 50]:

$$|\Omega_L\rangle = \prod_{\text{Re}(E_m) < E_F} d_{Lm}^\dagger |0\rangle, \quad |\Omega_R\rangle = \prod_{\text{Re}(E_n) < E_F} d_{Rn}^\dagger |0\rangle. \quad (3)$$

The biorthogonal density matrix of the ground state is defined as  $\rho^{RL} = |\Omega_R\rangle\langle\Omega_L|$ , which in general is neither Hermitian nor positive-definite [38]. If partitioning the total system into two subsystems  $A$  and  $B$  and tracing out all degrees of freedom in subsystem  $B$ , one can obtain

the reduced density matrix  $\rho_A^{RL} = \text{Tr}_B \rho^{RL}$ . Following the definitions for Hermitian system, the von-Neumann entanglement entropy is given by [28, 29, 38]

$$S_A = -\text{Tr} \left[ \rho_A^{RL} \log(\rho_A^{RL}) \right], \quad (4)$$

and the  $\alpha$ -order of Rényi entropy is

$$S_A^\alpha = \frac{1}{1-\alpha} \log \text{Tr} \left[ (\rho_A^{RL})^\alpha \right] \quad (5)$$

with  $\lim_{\alpha \rightarrow 1} S_A^\alpha = S_A$ . The entanglement entropy can be computed using the method of correlation matrix [51–53]. For free non-Hermitian Fermions, the biorthogonal correlation matrix  $C^A$  of subsystem  $A$  is defined as [28, 29, 36]

$$C_{ij}^A = \text{Tr}(\rho_A^{RL} c_i^\dagger c_j) = \langle \Omega_L | c_i^\dagger c_j | \Omega_R \rangle = \sum_{m \in \text{occ.}} W_{mi}^\dagger V_{jm}, \quad (6)$$

in which the sites  $i, j$  are restricted inside the subsystem  $A$  and the index  $m$  labels the occupied energy levels. The single-particle entanglement spectrum is obtained from the eigenvalue spectrum  $\{\xi_l\}$  of the matrix  $C^A$  under periodic boundary condition. Based on this, the von-Neumann and Rényi entropy are given by

$$S_A = -\sum_l (\xi_l \log(\xi_l) + (1 - \xi_l) \log(1 - \xi_l)), \quad (7)$$

$$S_A^\alpha = \frac{1}{1-\alpha} \sum_l \log((1 - \xi_l)^\alpha + \xi_l^\alpha). \quad (8)$$

The definition of edge entanglement entropy  $S_{\text{edge}}^\alpha$  reads

$$S_{\text{edge}}^\alpha = S_{\text{OBC}}^\alpha - \frac{1}{2} S_{\text{PBC}}^\alpha, \quad (9)$$

where  $S_{\text{OBC}}^\alpha$  and  $S_{\text{PBC}}^\alpha$  are  $\alpha$ -th Rényi entropies calculated under OBC and PBC, respectively. The edge entanglement entropy is a useful tool to extract the topological information of edge states [30, 50, 54].

To study the critical behavior of non-Hermitian systems, the entanglement entropy can be fitted using the following universal formula [55, 56],

$$S_A^\alpha(L_A) = \frac{c}{6} \left( 1 + \frac{1}{\alpha} \right) \ln \left( \frac{L}{\pi} \sin \left[ \frac{\pi L_A}{L} \right] \right) + a_\alpha, \quad (10)$$

in which  $c$  is the central charge described by conformal field theory (CFT),  $a_\alpha$  is a non-universal constant,  $L(L_A)$  is the length of system (subsystem  $A$ ), and  $\alpha$  is the order of Rényi entropy (for the von-Neumann entropy,  $\alpha = 1$ ). In Eq. (10), the total system length  $L$  is fixed and subsystem length  $L_A$  is variable. Another way to fit the entanglement entropy is to fix the ratio  $L_A/L = 1/2$  (equal bipartition),

$$S_A^\alpha(L) = \frac{c}{6} \left( 1 + \frac{1}{\alpha} \right) \ln(L) + b_\alpha, \quad (11)$$

in which  $b_\alpha$  is also a non-universal constant. Both fitting methods are used in this paper.

### III. QUASI-RECIPROCAL HAMILTONIAN BASED ON GENERALIZED BRILLOUIN ZONE

We consider a typical non-Hermitian SSH model with the following Bloch Hamiltonian [3, 57]

$$h(k) = \begin{pmatrix} 0 & (t_1 + \gamma) + t_2 e^{-ik} + t_3 e^{ik} \\ (t_1 - \gamma) + t_2 e^{ik} + t_3 e^{-ik} & 0 \end{pmatrix}, \quad (12)$$

in which  $k \in [0, 2\pi)$  being the crystal momentum. The hopping processes of this model in real space are illustrated in Fig. 1(a). According to the theory of GBZ [3, 16, 17], we substitute  $e^{ik}$  with  $\beta = e^{ik'}$  ( $k' = k + i\tau(k) \in \mathbb{C}$ ) to gain the corresponding non-Bloch Hamiltonian

$$h(\beta) = \begin{pmatrix} 0 & (t_1 + \gamma) + t_2 \beta^{-1} + t_3 \beta \\ (t_1 - \gamma) + t_2 \beta + t_3 \beta^{-1} & 0 \end{pmatrix}. \quad (13)$$

The characteristic equation of  $h(\beta)$  is given by

$$\det[E - h(\beta)] = 0, \quad (14)$$

which is a quartic equation and has four solutions  $\beta_i$  ( $i = 1, \dots, 4$ ) for a specific energy  $E$ . If ordering the solutions by their norms,  $|\beta_1(E)| \leq |\beta_2(E)| \leq |\beta_3(E)| \leq |\beta_4(E)|$ , the GBZ  $C_\beta$  is determined by the condition [3, 16, 17],

$$|\beta_2(E)| = |\beta_3(E)|. \quad (15)$$

Two typical GBZs are shown in Fig. 2(a) and (b), where the GBZ forms a closed loop encircling the origin on the complex plane. The OBC spectrum in the thermodynamic limit can be exactly obtained when  $\beta$  goes along the loop of GBZ.

To define the entanglement entropy in terms of GBZ, one need to construct an artificial real-space lattice which respects the translation invariance. Suppose that the phase angle of  $\beta_{GBZ}$  is equally distributed on the GBZ, we then construct non-Bloch Hamiltonian matrix  $H(\beta_{GBZ})$  by selecting the points whose phase angle belongs to the Brillouin zone (BZ) of original physical lattices, that is,

$$\text{Arg}(\beta_{GBZ}) = k_m = \frac{2\pi}{N}(m-1), \quad m = 1, \dots, N \quad (16)$$

where  $N$  is the number of unit cells of the lattice. The non-Bloch operator  $c_{\beta(k_m)}^\dagger$  can be transformed into a new lattice operator  $\tilde{c}_j$  by a Fourier transformation,

$$\tilde{c}_j^\dagger = \sum_m c_{\beta(k_m)}^\dagger U_{mj}, \quad U_{mj} = \frac{1}{\sqrt{N}} e^{-ik_m r_j}. \quad (17)$$

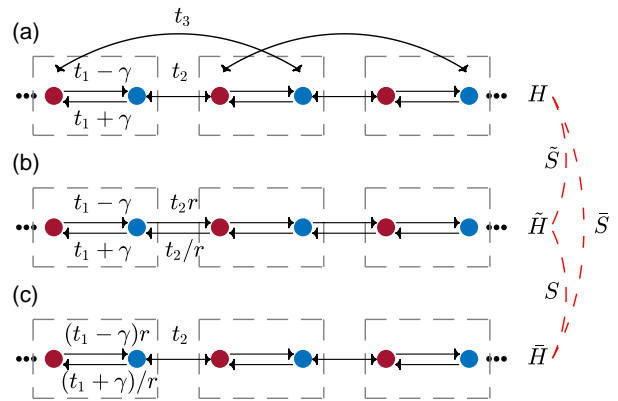


FIG. 1. (a) Schematic diagram of the non-Hermitian SSH model. (b) The quasi-reciprocal model when  $t_3 = 0$ , obtained by applying the similarity transformation  $\tilde{S}$  to the original non-Hermitian SSH model. (c) The model after the similarity transformation  $\tilde{S}$ .

After that, we obtain an "artificial" lattice Hamiltonian,

$$\tilde{H}_{PBC} = U^\dagger H(\beta_{GBZ}) U. \quad (18)$$

This type of Hamiltonian was previously studied in Ref. [48], which is named by quasi-reciprocal surrogate Hamiltonian there. The advantage of Hamiltonian  $\tilde{H}$  is that it is free of non-Hermitian skin effects, and therefore the concepts, developed for Hermitian (reciprocal) systems, may also be applicable to it. In this paper, we are particularly interested in the behavior of EE on this quasi-reciprocal lattice.

In principle, the quasi-reciprocal Hamiltonian  $\tilde{H}_{PBC}$  gives the OBC spectrum of a system ( $H_{OBC}$ ) in the thermodynamic limit, except for the isolated topological modes [16]. One can construct the OBC Hamiltonian  $\tilde{H}_{OBC}$  for the quasi-reciprocal lattice accordingly. For the bulk energy spectrum, we have

$$\{\epsilon_{OBC}\} \stackrel{N \rightarrow \infty}{\cong} \{\tilde{\epsilon}_{OBC}\} \stackrel{N \rightarrow \infty}{\cong} \{\tilde{\epsilon}_{PBC}\} \quad (19)$$

When next-nearest-neighbor (NNN) hoppings are included in the non-Hermitian SSH model, the degree of polynomial  $\det[E - H(\beta)]$  is greater than 2, and the GBZ will become non-circular [3]. In this case, the module  $|\beta|$  is not a constant but depends on the phase angle  $k$ . By Fourier transformation, this leads to the long-range hoppings in quasi-reciprocal lattices [48]. In practical calculations, we adopt an approximation to obtain the open boundary of quasi-reciprocal lattice: we neglect all the hopping terms whose hopping range is larger than half of the lattice length ( $N/2$ ). This is reasonable since long-range hoppings are generically power-law decaying [48].

A comparison of energy spectra for  $H_{OBC}$  and  $\tilde{H}_{OBC}$  is presented in Fig. 2(c) and (d). For circular GBZ, the quasi-reciprocal lattices possess exactly the same OBC spectra as the original lattice, no matter what lattice length  $L$  is. This can be understood by examining the

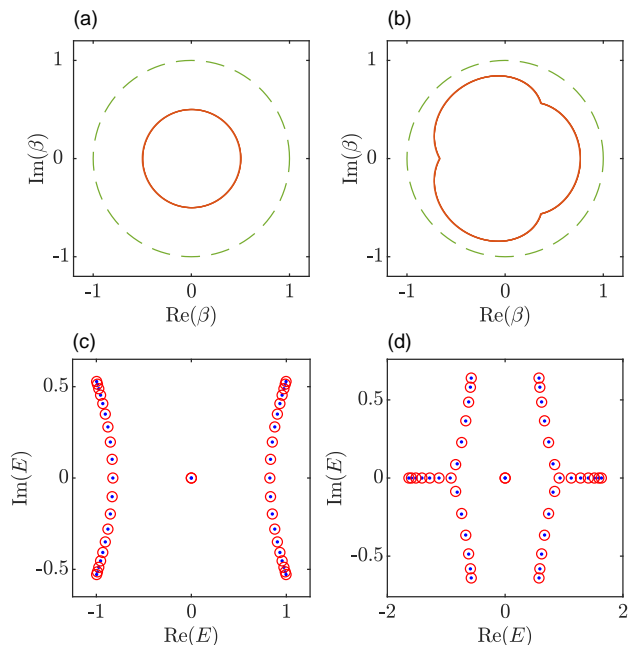


FIG. 2. The examples of circular GBZ (a) and non-circular GBZ (b). The green dashed circle denotes the conventional BZ with  $|\beta| = 1$ . The radius of circular GBZ (orange circle) in (a) is everywhere smaller than 1, indicating that wave functions only accumulate at the left end of the chain. Sub-figures (c) and (d) show the energy spectra of original OBC Hamiltonian  $H_{OBC}$  (blue dots) and quasi-reciprocal OBC Hamiltonian  $\tilde{H}_{OBC}$  (red circles). The length of lattice is set to be  $L = 40$ . For the case of circular GBZ (c), the blue dots precisely match the red circles. However, for the non-circular GBZ (d), the blue dots slightly deviate from the red circles, especially close to the bifurcations. We fix  $t_3 = 0$  in (a) and (c), but  $t_3 = 0.2$  in (b) and (d). Other parameters used in the calculations are  $t_1 = 0.4$ ,  $t_2 = 1$ , and  $\gamma = 2/3$ .

structure of  $h(\beta)$  in Eq. (13). When  $t_3 = 0$ , the module  $|\beta| = r$  is a constant, therefore  $h(\beta)$  and  $h(k)$  share the same form, except that the value of  $t_2$  is renormalized. The corresponding quasi-reciprocal lattices are shown in Fig. 1(b). In fact, the quasi-reciprocal Hamiltonian  $\tilde{H}_{OBC}$  is related to the original Hamiltonian  $H_{OBC}$  by a similarity transformation,

$$\tilde{H}_{OBC} = \tilde{S}^{-1} H_{OBC} \tilde{S}, \quad (20)$$

with  $\tilde{S} = \text{diag}\{r, r, r^2, r^2, \dots, r^{N-1}, r^N, r^N\}$ . This transformation differs from the well-studied similarity transformation  $\bar{S} = \text{diag}\{1, r, r, r^2, \dots, r^{N-1}, r^N\}$  [3], which renormalizes the intracell hopping amplitudes; see Fig. 1(c).

If  $t_3 \neq 0$ , the long-range hoppings appears in the quasi-reciprocal lattices due to the non-constant  $|\beta|$ . There are tiny difference between the energy spectra of  $H_{OBC}$  and  $\tilde{H}_{OBC}$  [see Fig. 2(d)], for the long-range hoppings can not be fully taken into account when the length of lattices is finite. The difference in energy spectra will decrease to zero in the thermodynamic limit.

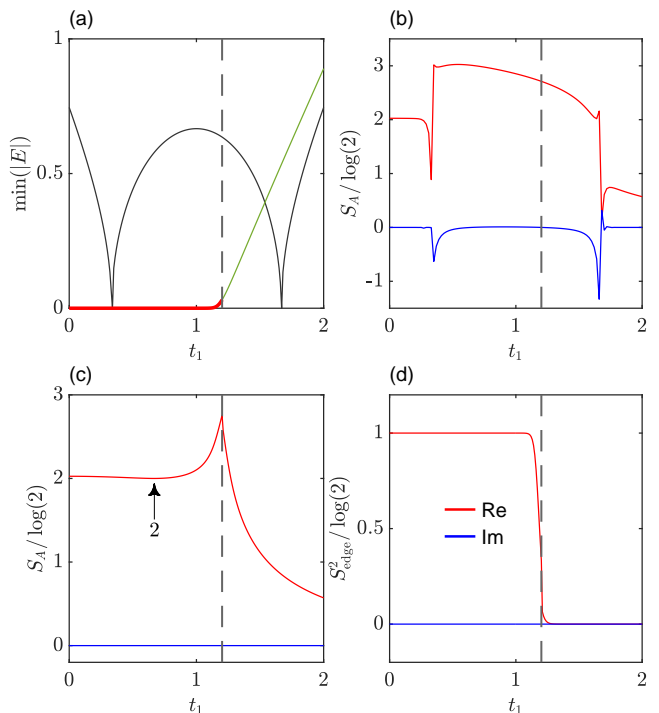


FIG. 3. (a) The minimum of absolute energy spectra  $|E|$  of the original lattices under PBC (black) and OBC (green) conditions. The red line denotes the topological zero-energy mode. The von Neumann entropy  $S_A$  of the original lattices and the quasi-reciprocal lattices are displayed in (b) and (c), respectively. Subfigure (d) shows the edge entropy of the quasi-reciprocal lattice with  $\alpha = 2$ . The real part of entropy is depicted in red, while the imaginary part is in blue. Parameters in the calculations are set to be  $t_2 = 1$ ,  $t_3 = 0$ ,  $\gamma = 2/3$ , and  $L = 100$ . The topological transition occurs at  $t_1 \simeq 1.202$  and is marked by the black dashed line.

#### IV. ENTANGLEMENT ENTROPY ON CIRCULAR GBZ

We first present the results of circular GBZ in Fig. 3, in which we use the non-Hermitian SSH model with  $t_3 = 0$  as an example. It is well-known that the BBC is broken in the non-Hermitian SSH model: the topological transition of zero-energy modes under OBC can not be explained by the Bloch Hamiltonian  $h(k)$  under PBC [3, 16]; see Fig. 3(a). The entanglement entropy can be calculated by applying the correlation matrix method described in Sec. II to the original non-Hermitian Hamiltonian under PBC [28, 29]. We show the results of entanglement entropy for SSH model with  $t_3 = 0$  in Fig. 3(b). The entanglement entropy is well-defined in the line-gap region, *i.e.*, the values are real and positive-definite (away from the two exceptional points). However, in the point-gap region, the entanglement entropy is not well-defined: it becomes complex with a non-zero imaginary part [28, 50]. Noted that at the special point with  $t_1 = t_2$  in the point-gap region, the entanglement entropy is also real, as studied in Ref. [36]. In all, the entanglement entropy defined on the

original PBC lattice basically reflects the characteristics of the Bloch band, and does not respect the BBC.

Hence, we propose to calculate the entanglement entropy using the quasi-reciprocal lattices defined in Eq. (18), which we term as the entanglement entropy on GBZ or the non-Bloch entanglement entropy. As displayed in Fig. 3(c), interestingly, the von Neumann entropy  $S_A$  is well-defined across the parameter space: it is positive-definite and real with zero imaginary part. It also diverges at the topological transition points (see the black dashed line), thus recovering the BBC. The edge entropy, plotted in Fig. 3(d), is quantized at 1 (in units of  $\log(2)$ ) within the topological phase, and changes to zero at the topological transition point.

The entanglement entropy drops to  $2\log(2)$  at the point  $t_1 = \gamma$ ; see Fig. 3(c). At this point, the GBZ collapses into a single point with  $r = 0$ , and the intra-(inter-)unit cell hoppings of the quasi-reciprocal lattice become  $2\gamma$  and  $0$  ( $0$  and  $\infty$ ), respectively. By performing the similar transformation  $S = \text{diag}\{1, 1/r, 1, 1/r, \dots, 1, 1/r\}$ , this case can be mapped into the dimerized limit with intra-unit cell hopping being zero; see Fig. 1(c). There are two isolated edge states, hence the entanglement entropy is exactly  $2\log(2)$  [58]. Note, when  $t_1 < \gamma$ , the Hamiltonian  $H$  cannot be transformed into an Hermitian SSH model [3]. However, the entropy remains well-defined, as demonstrated in Fig. 3(c); see the Appendix A for the analysis of realness. This is a significant finding of the present paper.

The quasi-reciprocal lattice Hamiltonian has an EP at  $\gamma_c = \sqrt{t_1^2 + t_2^2}$ . We then turn to study the possible critical behavior in this model. In Fig. 4(a), the fitted  $c$  is plotted as a function of  $\gamma$  for  $t_1 = 0.5$ . For  $\gamma < \gamma_c$ , the value of  $c$  is zero, indicating that the system is non-critical in this region. However, for  $\gamma > \gamma_c$ , the value of  $c$  saturates to 2, implying critical behavior; See Fig. 4(b) for the representative logarithmic scaling of entanglement entropy with  $L_A/L = 1/2$ . The critical behavior is associated with the Fermi surface structure of the energy spectrum [36]. Since we construct the ground state according to the real part of energy, the system is an insulator without any Fermi points when  $\gamma < \gamma_c$ , but when  $\gamma > \gamma_c$  it becomes a gapless metal with two Fermi points. We therefore conclude that each Fermi point contributes exactly 1 to the central charge  $c$  of the logarithmic scaling. This is different from the original SSH model (PBC) studied in Ref. [36], where each Fermi point contributes  $1/2$  to the value of  $c$ .

The entanglement entropy diverges at the EP with  $\gamma = \gamma_c$ . The insets in Fig. 4(c) shows the two exceptional momentum  $k_{EP}$  ( $0$  and  $\pi$ ) in this model. To avoid divergence, the entanglement entropy can be calculated by slightly shifting from the EP  $\gamma = \gamma_c - \eta$  [29, 38]. Note that the dispersion of this EP is square root dependence on  $k$  instead of linear. The scaling behavior of entanglement entropy for a fixed system length  $L = 400$  is shown in Fig. 4(d), where a tiny shift  $\eta = 1 \times 10^{-8}$  is used and  $L_A$  is chosen to include an odd number of unit

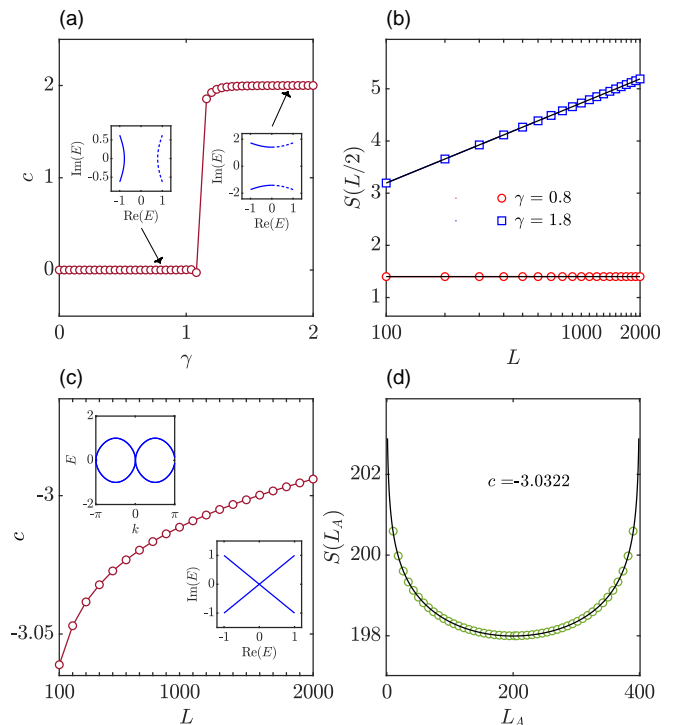


FIG. 4. (a) The central charges of entanglement entropy (real) on circular GBZ as a function of  $\gamma$ . The two insets display representative energy spectra on two sides of the EP  $\gamma_c = \sqrt{1.25}$ , where the solid (dashed) line indicate the occupied (unoccupied) states. (b) The logarithmic scaling of entanglement entropy (fixed ratio  $L_A/L = 1/2$ ) when  $\gamma$  is far away from EP. (c) The fitted central charge using Eq. (10) versus total system length  $L$ . In the calculations,  $\gamma$  is shifted from  $\gamma_c$  by a tiny quantity  $\eta = 1 \times 10^{-8}$ . Insets display the energy spectrum and the dispersion relation, revealing two exceptional momenta at  $k = 0, \pi$  that render the momentum-space Hamiltonian defective. (d) The entanglement entropy as a function of the subsystem length  $L_A$  for fixed total length  $L = 400$ . The hopping parameters for all sub-figures are  $t_1 = 0.5$ ,  $t_2 = 1$ , and  $t_3 = 0$ .

cells. The extracted central charge is negative (around  $-3$ ), which is attributed to the exceptional bound state close to EP [37]. However, the value of central charge slightly increases when the system length is increasing, as depicted in Fig. 4(c).

## V. ENTANGLEMENT ENTROPY ON NON-CIRCULAR GBZ

We now consider the general cases of non-circular GBZ, where long-range hopping appears in the quasi-reciprocal lattices. The entanglement entropy calculated on the quasi-reciprocal lattices is presented in Fig. 5 for the case of  $t_3 = 0.2$ . The von Neumann entropy exhibits singularity at the topological transition point, similar to the circular GBZ case in Fig. 3(c). However, it is not well-defined (*i.e.*, becomes complex valued) anymore in

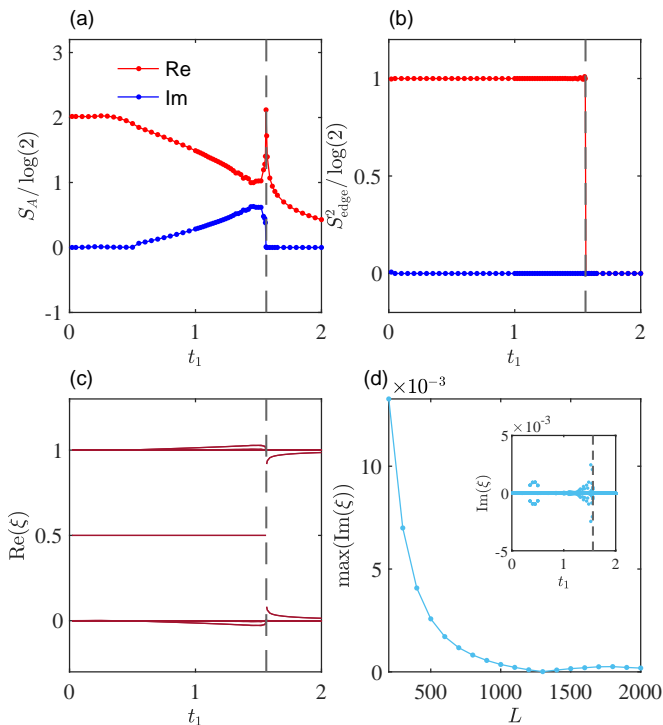


FIG. 5. The von Neumann (a) and  $\alpha = 2$  edge (b) entanglement entropy, calculated on the quasi-reciprocal lattice, are plotted as a function of  $t_1$ . Real and imaginary parts of entropy are shown in red and blue color, respectively. (c) The real part of the entanglement spectrum  $\xi$  as a function of  $t_1$ . (d) The maximum imaginary part of entanglement spectrum at  $t_1 = 1.45$  varies as a function of system length  $L$ . It decreases to a small value once  $L$  becomes sufficiently large. The inset shows the imaginary of the entanglement spectrum. The topological transition occurs at  $t_{1c} = 1.562$  and is denoted by the black dashed line. The values of parameters used in the calculations are  $\gamma = 2/3$ ,  $t_2 = 1$ ,  $t_3 = 0.2$  and  $L = 800$ .

the topological region with  $t_1 < t_{1c}$ . As shown in Fig. 5(c), the values of entanglement spectrum go outside the bound  $[0, 1]$ , which leads to an imaginary part in the von Neumann entanglement entropy.

However, the behavior of the edge entanglement entropy is significant: as shown in Fig. 5(b), it retains real ( $L \rightarrow \infty$ ), quantized values of 1 in the topological region, but then drops to zero upon entering the topologically trivial region. This means that the edge entanglement entropy is a good topological indicator, able to recover the BBC, even in the case of non-circular GBZ.

The phase diagram of quasi-reciprocal Hamiltonian is shown in Fig. 6. A gapless semimetal phase (Phase II) appears when  $t_3 \neq 0$ , in which the system becomes exceptional. We then consider possible scaling behaviors along the boundaries delineating this exceptional phase [43]. Since the von Neumann entropy  $S_A$  is complex, we adopt the generalized entanglement entropy  $S_A^g$ , proposed in Ref. [38], to investigate the critical properties,

$$S_A^g = -\text{tr}_B(\rho_A^{\text{RL}} \log(|\rho_A^{\text{RL}}|)), \quad (21)$$

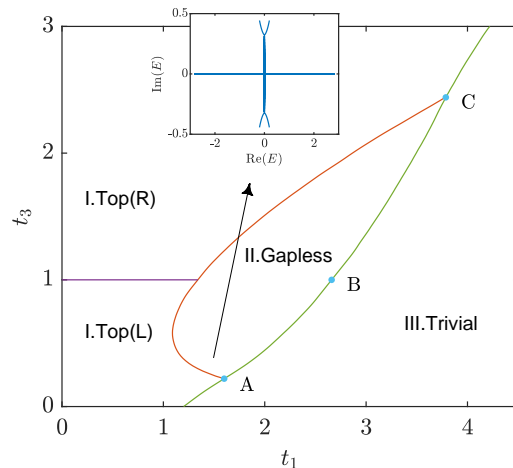


FIG. 6. Phase diagram of the non-Hermitian SSH model under OBC in the  $t_1-t_3$  plane. Phase I is the gapped topological phase. The letters  $L$  and  $R$ , abbreviating "left" and "right", indicate the accumulating direction of skin modes. Phase II is the gapless semimetal phase, with the gap closing at some exceptional momentum points. A typical energy spectrum is shown in the inset. The phase boundaries around Phase II are all exceptional. Phase III is the gapped topologically trivial phase. The parameters used in the calculations are  $\gamma = 2/3$ ,  $t_2 = 1$ ,  $L = 200$ .

which in terms of the entanglement spectrum can be written as

$$S_A^g = -\sum_l (\xi_l \log(|\xi_l|) + (1 - \xi_l) \log(|1 - \xi_l|)). \quad (22)$$

The central charges can be obtained as usual by fitting the generalized entropy  $S_A^g$  to the scaling formulas given in Eqs. (10) and (11).

To avoid the singularity at  $k_{EP}$ , we introduce a tiny momentum shift  $\delta$  [38] and choose the momentum as  $k = k_m + \delta/N$ , with  $k_m$  being the ordinary momentum in Eq. (16). The fitted central charges along the topological-trivial and the semimetal-trivial phase boundaries (the green line in Fig. 6) are plotted in Fig. 7(a), where a tiny shift  $\delta = 1 \times 10^{-4}$  is used. For  $t_3 = 0$ , the quasi-reciprocal model can be mapped to the Hermitian SSH model (see Fig. 1(c)), so that the central charge at the topological transition point is  $c = 1$ . The value of  $c$  decreases slightly from 1 when approaching the tri-critical point  $A$ . Upon entering the exceptional region, the value of  $c$  drops to a negative value (around  $-2$ ), which is governed by the exceptional bound state [37]. At the critical point  $B$  with  $t_3 = t_2 = 1$  and  $t_1 = 2 + \gamma$ , the GBZ is a circle with  $|\beta| = 1$ . The momentum-space Hamiltonian in the vicinity of the exceptional momentum  $k_{EP} = \pi$  can be written as

$$H(k_{EP} + k) = \begin{pmatrix} 0 & 2\gamma + k^2 \\ k^2 & 0 \end{pmatrix}, \quad (23)$$

which exhibits a linear dispersion. This Hamiltonian is a minimal exceptional bound state model [37], and the

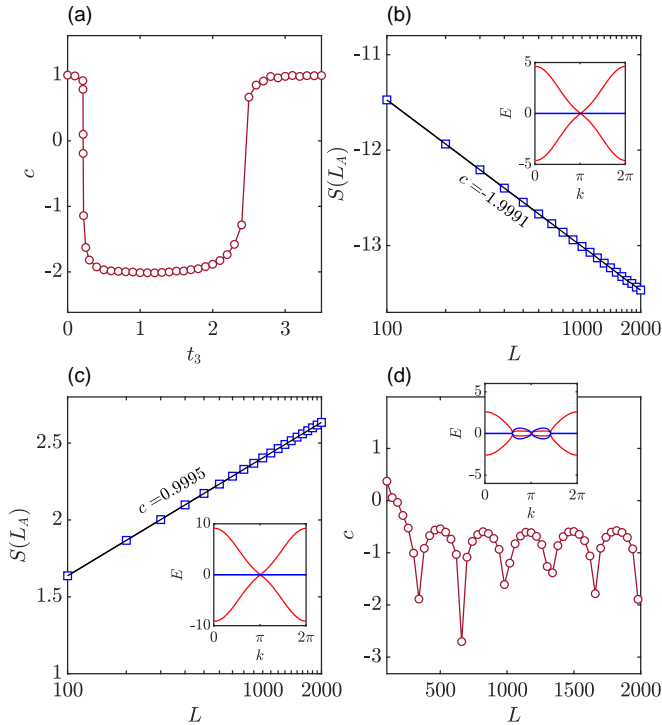


FIG. 7. (a) The fitted central charges are plotted along the green line in Fig. 6, which delineates the boundaries between the topological phase (the semimetal phase) and the trivial phase. The parameters used in the calculations are  $\gamma = 2/3$ ,  $t_2 = 1$ ,  $L = 200$ . (b) The logarithmic scaling of generalized entanglement entropy at point  $B$  in Fig. 6 with  $t_1 = 8/3$  and  $t_3 = t_2 = 1$ . (c) The logarithmic scaling of generalized entanglement entropy at  $t_1 = 4.65725241$  and  $t_3 = 3.5$ . (d) The fitted central charge as a function of system length  $L$  at  $t_1 = 1.08907404$  and  $t_3 = 0.6$  (on the topological-semimetal phase boundary). In all sub-figures, a momentum shift  $\delta = 1 \times 10^{-4}$  is used in the calculations. The insets in (b), (c), and (d) show the dispersion relations, where the real and imaginary part of energy are plotted in red and blue color, respectively.

central charge is precisely  $-2$  at this point [37, 38], as illustrated in Fig. 7(b) with  $\delta = 1 \times 10^{-4}$ . For the other points on the semimetal-trivial phase boundary different from point  $B$ , the dispersion deviates from being exactly linear, therefore the central charge deviates from the value of  $-2$  (*i.e.*, not an integer); see Fig. 7(a). When passing through the tri-critical point  $C$  along the phase boundary, the central charge becomes positive ( $c \approx 1$ ) again; see Fig. 7(c).

The situation of the topological-semimetal phase boundary (red line in Fig. 6) is more intricate. On the boundary delimiting the topologically trivial phase (the green line in Fig. 6), the exceptional momentum  $k_{EP}$  is at  $\pi$ . However, on the topological semimetal phase boundary, two additional exceptional momenta different from 0 or  $\pi$  appear, as depicted in the inset of Fig. 7(d). Depending on the length of the system, it is possible that the crystal momentum does not coincide with  $k_{EP}$ . This

renders the calculation of the central charge challenging. For a given length  $L$ , we employ the formula of Eq. (10) to obtain the fitted central charges, and then plot them as a function of  $L$  in Fig. 7(d). Evidently, the fitted central charge  $c$  exhibits an oscillatory behavior.

## VI. SUMMARY AND DISCUSSION

We introduce the quasi-reciprocal Hamiltonian and lattice in real space, which is obtained by performing a regular Fourier transformation on the non-Bloch Hamiltonian. We calculate the entanglement entropy on these quasi-reciprocal lattices, and term it as the non-Bloch entanglement entropy. Since the quasi-reciprocal lattice is free of skin effect, the non-Bloch entanglement entropy exhibits well-behaved characteristics. For cases where the GBZ is circular, the non-Bloch entanglement entropy is shown to be well-defined (real and positive-definite). The non-Bloch entanglement entropy exhibits a logarithmic scaling in the critical region. It is found that the critical behavior is associated with the Fermi surface structure of the energy spectrum: each Fermi point contributes precisely 1 to the central charge  $c$  of the logarithmic scaling. At the exceptional point, the central charge becomes negative due to the presence of the exceptional bound state. When the GBZ is non-circular, the non-Bloch von Neumann entropy becomes complex-valued in the topological region, due to the emergence of long-range hopping in the quasi-reciprocal lattice. Nonetheless, the non-Bloch edge entanglement entropy remains real and quantized, thus serving as a reliable topological indicator recovering the BBC. Furthermore, We computes the topological phase diagram and reveals the critical behavior along exceptional phase boundaries between topological, semimetal, and trivial phases. The central charge exhibits interesting behaviors, such as becoming precisely  $-2$  at the critical point with  $t_3 = t_2$  or oscillating as a function of the system's length on the topological-semimetal phase boundary. Overall, this study sheds new light on the physical meanings of the GBZ and non-Hermitian entanglement entropy, opening new possibilities for studying many-body physics based on the GBZ.

Finally, we emphasize that the non-Bloch entanglement entropy accurately characterizes the entanglement behavior of the original non-Hermitian systems under OBC. Motivated by the successful measurement of entanglement entropy in Hermitian phononic systems [59], we anticipate that the non-Bloch entanglement entropy can be experimentally identified and measured in future endeavors.

## ACKNOWLEDGMENT

We are grateful for the discussions with Zhesen Yang, Hantao Lu, and Shijie Hu. This work is supported by the

National Natural Science Foundation of China (Grants No. 11974293).

*Note added.* After completing our work, we became aware of a preprint [61] whose findings partially overlap with ours.

### Appendix A: The realness of entanglement entropy for circular GBZ

The correlation matrix  $C$  is a projection that projects onto the occupied band:  $C^2 = C$ . However, the truncated correlation matrix  $C^A$ , which is related to the entanglement spectrum, is not a projection [37, 60]. We therefore focus on the quantity  $C_{\text{mix}} = C_A - C_A^2$  to investigate the realness of entanglement entropy [37]. An eigenstate  $|\psi\rangle$  of  $C_A$  with eigenvalue  $\xi$  is also an eigenstate of  $C_{\text{mix}}$  with eigenvalue  $\xi(1-\xi)$ . For a single entanglement cut, the correlation matrix  $C$  can be decomposed into four parts

$$C = \begin{pmatrix} C^A & C^{AB} \\ C^{BA} & C^B \end{pmatrix}. \quad (\text{A1})$$

Introducing a real-space projector  $P_A$  onto subsystem  $A$

$$P_A = \begin{pmatrix} 1_A & 0 \\ 0 & 0 \end{pmatrix} \quad (\text{A2})$$

it is straightforward to show that

$$(P_A C P_A)^2 - P_A C P_A = P_A C [P_A, C] P_A, \quad (\text{A3})$$

that is,

$$\begin{pmatrix} C_A^2 - C_A & 0 \\ 0 & 0 \end{pmatrix} = \begin{pmatrix} -C_{AB} C_{BA} & 0 \\ 0 & 0 \end{pmatrix} \quad (\text{A4})$$

Therefore, we obtain  $C_{\text{mix}} = C_{AB} C_{BA}$ .

We consider the two-band non-Bloch Hamiltonian in Eq. (13) with circular GBZ (*i.e.*,  $t_3 = 0$ ),

$$h(\beta) = \begin{pmatrix} 0 & h_+(\beta_k) \\ h_-(\beta_k) & 0 \end{pmatrix} \quad (\text{A5})$$

where  $h_+(\beta_k) = (t_1 + \gamma) + t_2 e^{-ik}/r$ ,  $h_-(\beta_k) = (t_1 - \gamma) + t_2 r e^{ik}$ , and  $|\beta_k| = r = \sqrt{|(t_1 - \gamma)/(t_1 + \gamma)|}$  is a constant. For a half-filled system, correlation matrix in momentum-space representation is given by [37]

$$P(k) = \frac{1}{2} \begin{pmatrix} 1 & -h_+(\beta_k)/\varepsilon(\beta_k) \\ -h_-(\beta_k)/\varepsilon(\beta_k) & 1 \end{pmatrix}, \quad (\text{A6})$$

where  $\varepsilon(\beta_k) = \sqrt{h_+(\beta_k)h_-(\beta_k)}$  is the positive root. The block element of correlation matrix in real space can be obtained by a Fourier transformation [37],

$$\begin{aligned} C_{ij} &= \langle x_i | P | x_j \rangle = \frac{1}{N} \sum_k e^{ik(x_i - x_j)} P(k) \\ &= \begin{pmatrix} \frac{1}{2} \delta_{x_i, x_j} & f_+(x_i - x_j) \\ f_-(x_i - x_j) & \frac{1}{2} \delta_{x_i, x_j} \end{pmatrix}, \end{aligned} \quad (\text{A7})$$

where

$$f_{\pm}(x) = -\frac{1}{2N} \sum_k e^{ikx} \frac{h_{\pm}(\beta_k)}{\varepsilon(\beta_k)}, \quad (\text{A8})$$

and  $N$  is the number of unit cells. Note that  $f_{\pm}(x)$  is always a real number for any value of  $x$ , since

$$\frac{h_{\pm}(\beta_k)}{\varepsilon(\beta_k)} \equiv \left[ \frac{h_{\pm}(\beta_{-k})}{\varepsilon(\beta_{-k})} \right]^* \quad (\text{A9})$$

Then, the matrix  $C_{\text{mix}}$  can be expressed as

$$\begin{aligned} (C_{\text{mix}})_{x_1, x_2} &= \sum_{x_3 \in B} C_{x_1, x_3} C_{x_3, x_2} = \begin{pmatrix} U & 0 \\ 0 & V \end{pmatrix} \\ U &= \sum_{x_3 \in B} f_+(x_1 - x_3) f_-(x_3 - x_2) \\ V &= \sum_{x_3 \in B} f_-(x_1 - x_3) f_+(x_3 - x_2), \end{aligned} \quad (\text{A10})$$

in which  $x_1$  and  $x_2$  denote the sites in subsystem  $A$ , while  $x_3$  denotes the sites in subsystem  $B$ . Clearly,  $C_{\text{mix}}$  is a real matrix.

#### 1. Case I: $t_1 > \gamma$

In this section, we demonstrate that  $C_{\text{mix}}$  is a Hermitian matrix with real eigenvalues in the region of  $t_1 > \gamma$ . For  $t_1 > \gamma$ , the following two conditions are satisfied,

$$h_+(\beta_{k_1}) h_-(\beta_{k_2}) \equiv h_+(\beta_{-k_2}) h_-(\beta_{-k_1}) \quad (\text{A11})$$

$$\varepsilon(\beta_{k_1}) \varepsilon(\beta_{k_2}) \equiv \varepsilon(\beta_{-k_2}) \varepsilon(\beta_{-k_1}). \quad (\text{A12})$$

Therefore, we have

$$\frac{h_+(\beta_{k_1})}{\varepsilon(\beta_{k_1})} \frac{h_-(\beta_{k_2})}{\varepsilon(\beta_{k_2})} \equiv \frac{h_+(\beta_{-k_2})}{\varepsilon(\beta_{-k_2})} \frac{h_-(\beta_{-k_1})}{\varepsilon(\beta_{-k_1})} \quad (\text{A13})$$

Combining Eq. (A13) with the definition of  $f_{\pm}(x)$  in Eq. (A8), we obtain,

$$f_+(y_1) f_-(y_2) \equiv f_+(-y_2) f_-(-y_1), \quad (\text{A14})$$

where  $y_1$  and  $y_2$  denote any positions on the lattice. By the relation in Eq. (A14), it is straightforward to show that

$$(C_{\text{mix}})_{x_1, x_2} = (C_{\text{mix}})_{x_2, x_1}. \quad (\text{A15})$$

Considering that  $C_{\text{mix}}$  is real, we thus conclude that  $C_{\text{mix}}$  is Hermitian when  $t_1 > \gamma$ . This validates the realness of the entanglement entropy in this region.



## 2. Case II: $t_1 < \gamma$

In the region  $t_1 < \gamma$ , the non-Hermitian SSH model without  $t_3$  can not be transformed into a Hermitian one through a similarity transformation [3]. In this case, the Eq. (A11) is no longer valid, and  $C_{\text{mix}}$  is no longer Hermitian. In the following, we illustrate the general properties of  $C_{\text{mix}}$  matrix using a simple example where the lattice has only four unit cells ( $N = 4$ ). When  $t_1 < \gamma$ , the general structure of  $C_{\text{mix}}$  is the sum of a skew-symmetric matrix and a diagonal matrix. For the  $N = 4$  case, it is

$$C_{\text{mix}} = \begin{pmatrix} a & 0 & c & 0 \\ 0 & b & 0 & c \\ -c & 0 & b & 0 \\ 0 & -c & 0 & a \end{pmatrix}, \quad (\text{A16})$$

which contains three different variables

$$a = f_+(2)f_-(2) + f_+(1)f_-(3) \quad (\text{A17})$$

$$b = f_+(2)f_-(2) + f_+(3)f_-(1) \quad (\text{A18})$$

$$c = f_+(3)f_-(2) + f_+(2)f_-(3) \quad (\text{A19})$$

The characteristic equation of  $C_{\text{mix}}$  is

$$\det(\lambda - C_{\text{mix}}) = \left[ \lambda^2 - (a + b)\lambda + (ab + c^2) \right]^2 = 0 \quad (\text{A20})$$

To solve this, we observe that the following auxiliary function

$$g(k_1, k_2) = \frac{h_+(k_1)h_-(k_2)}{\varepsilon(k_1)\varepsilon(k_2)} \quad (\text{A21})$$

takes values as in the table below

$k_1 \backslash k_2$	0	$\pi/2$	$\pi$	$3\pi/2$
0	1	$z$	$z^2$	$z^*$
$\pi/2$	$1/z$	1	$z$	-1
$\pi$	$1/z^2$	$1/z$	1	$1/z^*$
$3\pi/2$	$1/z^*$	-1	$z^*$	1

This table contains only one independent variable, namely  $z = g(0, \pi/2)$ . Combining this table and the definition in Eq. (A8), we obtain

$$a + b = \frac{1}{4} \quad (\text{A22})$$

$$ab + c^2 = 0 \quad (\text{A23})$$

which holds except at the exceptional point. Therefore, the eigenvalues  $\lambda$  of  $C_{\text{mix}}$  are 0, 0,  $1/4$ ,  $1/4$ , resulting in a real entanglement entropy with a precise value of  $2 \log(2)$ . When  $N > 4$ , the above table becomes much more complex. However, we numerically verify that the entanglement entropy is always real.

- 
- [1] Y. Ashida, Z. Gong, and M. Ueda, *Advances in Physics* **69**, 249 (2020).
- [2] E. J. Bergholtz, J. C. Budich, and F. K. Kunst, *Rev. Mod. Phys.* **93**, 015005 (2021).
- [3] S. Yao and Z. Wang, *Phys. Rev. Lett.* **121**, 086803 (2018).
- [4] Z. Yan, F. Song, and Z. Wang, *Phys. Rev. Lett.* **121**, 096803 (2018).
- [5] F. K. Kunst, E. Edvardsson, J. C. Budich, and E. J. Bergholtz, *Phys. Rev. Lett.* **121**, 026808 (2018).
- [6] C. H. Lee and R. Thomale, *Phys. Rev. B* **99**, 201103 (2019).
- [7] X. Zhang, T. Zhang, M.-H. Lu, and Y.-F. Chen, *Advances in Physics: X* **7**, 2109431 (2022), <https://doi.org/10.1080/23746149.2022.2109431>.
- [8] R. Lin, T. Tai, L. Li, and C. H. Lee, *Frontiers of Physics* **18**, 10.1007/s11467-023-1309-z (2023).
- [9] T. Tai and C. H. Lee, *Phys. Rev. B* **107**, L220301 (2023).
- [10] K. Zhang, Z. Yang, and C. Fang, *Phys. Rev. Lett.* **125**, 126402 (2020).
- [11] N. Okuma, K. Kawabata, K. Shiozaki, and M. Sato, *Phys. Rev. Lett.* **124**, 086801 (2020).
- [12] X.-L. Qi and S.-C. Zhang, *Rev. Mod. Phys.* **83**, 1057 (2011).
- [13] M. Z. Hasan and C. L. Kane, *Rev. Mod. Phys.* **82**, 3045 (2010).
- [14] T. E. Lee, *Phys. Rev. Lett.* **116**, 133903 (2016).
- [15] Y. Xiong, *Journal of Physics Communications* **2**, 035043 (2018).
- [16] K. Yokomizo and S. Murakami, *Phys. Rev. Lett.* **123**, 066404 (2019).
- [17] Z. Yang, K. Zhang, C. Fang, and J. Hu, *Phys. Rev. Lett.* **125**, 226402 (2020).
- [18] W.-T. Xue, M.-R. Li, Y.-M. Hu, F. Song, and Z. Wang, *Phys. Rev. B* **103**, L241408 (2021).
- [19] S. Longhi, *Phys. Rev. Res.* **1**, 023013 (2019).
- [20] L. Xiao, T. Deng, K. Wang, Z. Wang, W. Yi, and P. Xue, *Phys. Rev. Lett.* **126**, 230402 (2021).
- [21] L. Amico, R. Fazio, A. Osterloh, and V. Vedral, *Rev. Mod. Phys.* **80**, 517 (2008).
- [22] J. Eisert, M. Cramer, and M. B. Plenio, *Rev. Mod. Phys.* **82**, 277 (2010).
- [23] M. Levin and X.-G. Wen, *Phys. Rev. Lett.* **96**, 110405 (2006).
- [24] A. Kitaev and J. Preskill, *Phys. Rev. Lett.* **96**, 110404 (2006).
- [25] C. Holzhey, F. Larsen, and F. Wilczek, *Nuclear Physics B* **424**, 443 (1994).
- [26] P. Calabrese and J. Cardy, *Journal of Physics A: Mathematical and Theoretical* **42**, 504005 (2009).
- [27] R. Couvreur, J. L. Jacobsen, and H. Saleur, *Phys. Rev. Lett.* **119**, 040601 (2017).
- [28] L. Herviou, N. Regnault, and J. H. Bardarson, *SciPost Physics* **7**, 069 (2019).
- [29] P.-Y. Chang, J.-S. You, X. Wen, and S. Ryu, *Phys. Rev. Research* **2**, 033069 (2020).
- [30] E. Lee, H. Lee, and B.-J. Yang, *Phys. Rev. B* **101**, 121109 (2020).
- [31] S. Mu, C. H. Lee, L. Li, and J. Gong, *Phys. Rev. B* **102**,

- 081115 (2020).
- [32] L.-M. Chen, S. A. Chen, and P. Ye, *SciPost Phys.* **11**, 3 (2021).
- [33] N. Okuma and M. Sato, *Phys. Rev. B* **103**, 085428 (2021).
- [34] A. Bácsi and B. Dóra, *Phys. Rev. B* **103**, 085137 (2021).
- [35] R. Modak and B. P. Mandal, *Phys. Rev. A* **103**, 062416 (2021).
- [36] Y.-B. Guo, Y.-C. Yu, R.-Z. Huang, L.-P. Yang, R.-Z. Chi, H.-J. Liao, and T. Xiang, *J. Phys.: Condens. Matter* **33**, 475502 (2021).
- [37] C. H. Lee, *Phys. Rev. Lett.* **128**, 010402 (2022).
- [38] Y.-T. Tu, Y.-C. Tzeng, and P.-Y. Chang, *SciPost Phys.* **12**, 194 (2022).
- [39] L.-M. Chen, Y. Zhou, S. A. Chen, and P. Ye, *Phys. Rev. B* **105**, L121115 (2022).
- [40] M. Fossati, F. Ares, and P. Calabrese, *Phys. Rev. B* **107**, 205153 (2023).
- [41] K. Kawabata, T. Numasawa, and S. Ryu, *Phys. Rev. X* **13**, 021007 (2023).
- [42] X. Feng, S. Liu, S. Chen, and W. Guo, *Phys. Rev. B* **107**, 094309 (2023).
- [43] W.-Z. Yi, Y.-J. Hai, R. Xiao, and W.-Q. Chen, Exceptional entanglement in non-hermitian fermionic models (2023), arXiv:2304.08609 [quant-ph].
- [44] W. Pan, X. Wang, H. Lin, and S. Hu, Negative super-inflating bipartite fluctuations near exceptional points in  $\mathcal{PT}$ -symmetric models (2023), arXiv:2304.10368 [cond-mat.mes-hall].
- [45] Y.-C. Wang, H. H. Jen, and J.-S. You, *Phys. Rev. B* **108**, 085418 (2023).
- [46] C. Ortega-Taberner and M. Hermanns, *Phys. Rev. B* **107**, 235112 (2023).
- [47] C.-T. Hsieh and P.-Y. Chang, *SciPost Phys. Core* **6**, 062 (2023).
- [48] C. H. Lee, L. Li, R. Thomale, and J. Gong, *Phys. Rev. B* **102**, 085151 (2020).
- [49] D. C. Brody, *Journal of Physics A: Mathematical and Theoretical* **47**, 035305 (2013).
- [50] W. Chen, L. Peng, H. Lu, and X. Lu, *Phys. Rev. B* **105**, 075126 (2022).
- [51] I. Peschel, *Journal of Physics A: Mathematical and General* **36**, L205 (2003).
- [52] S.-A. Cheong and C. L. Henley, *Phys. Rev. B* **69**, 075111 (2004).
- [53] I. Peschel and V. Eisler, *Journal of Physics A: Mathematical and Theoretical* **42**, 504003 (2009).
- [54] D. Wang, S. Xu, Y. Wang, and C. Wu, *Phys. Rev. B* **91**, 115118 (2015).
- [55] P. Calabrese and J. Cardy, *Journal of Statistical Mechanics: Theory and Experiment* **2004**, P06002 (2004).
- [56] N. Laflorencie, *Physics Reports* **646**, 1 (2016).
- [57] S. Lieu, *Phys. Rev. B* **97**, 045106 (2018).
- [58] S. Ryu and Y. Hatsugai, *Phys. Rev. B* **73**, 245115 (2006).
- [59] Z.-K. Lin, Y. Zhou, B. Jiang, B.-Q. Wu, L.-M. Chen, X.-Y. Liu, L.-W. Wang, P. Ye, and J.-H. Jiang, *Nature Communications* **15**, 1601 (2024).
- [60] C. H. Lee and P. Ye, *Phys. Rev. B* **91**, 085119 (2015).
- [61] D. F. Muñoz-Arboleda, R. Arouca, and C. M. Smith, Thermodynamics and entanglement entropy of the non-hermitian ssh model (2024), arXiv:2406.13087.